FULL PAPER Open Access

Turbulent diffusion and volcanic gas dispersion in the atmospheric surface layer: insights from La Solfatara, Campi Flegrei, Italy

Check for updates

Silvia Massaro^{1,2*}, Giovanni Macedonio³, Giancarlo Tamburello¹, Manuel Stocchi², Francesco Rufino³, Stefano Caliro³, Giulio Bini¹, Alessandro Santi³, Rosario Avino³, Jacopo Selva⁴, Laura Sandri¹, Fabio Dioguardi^{2,5}, Giovanni Chiodini¹ and Antonio Costa¹

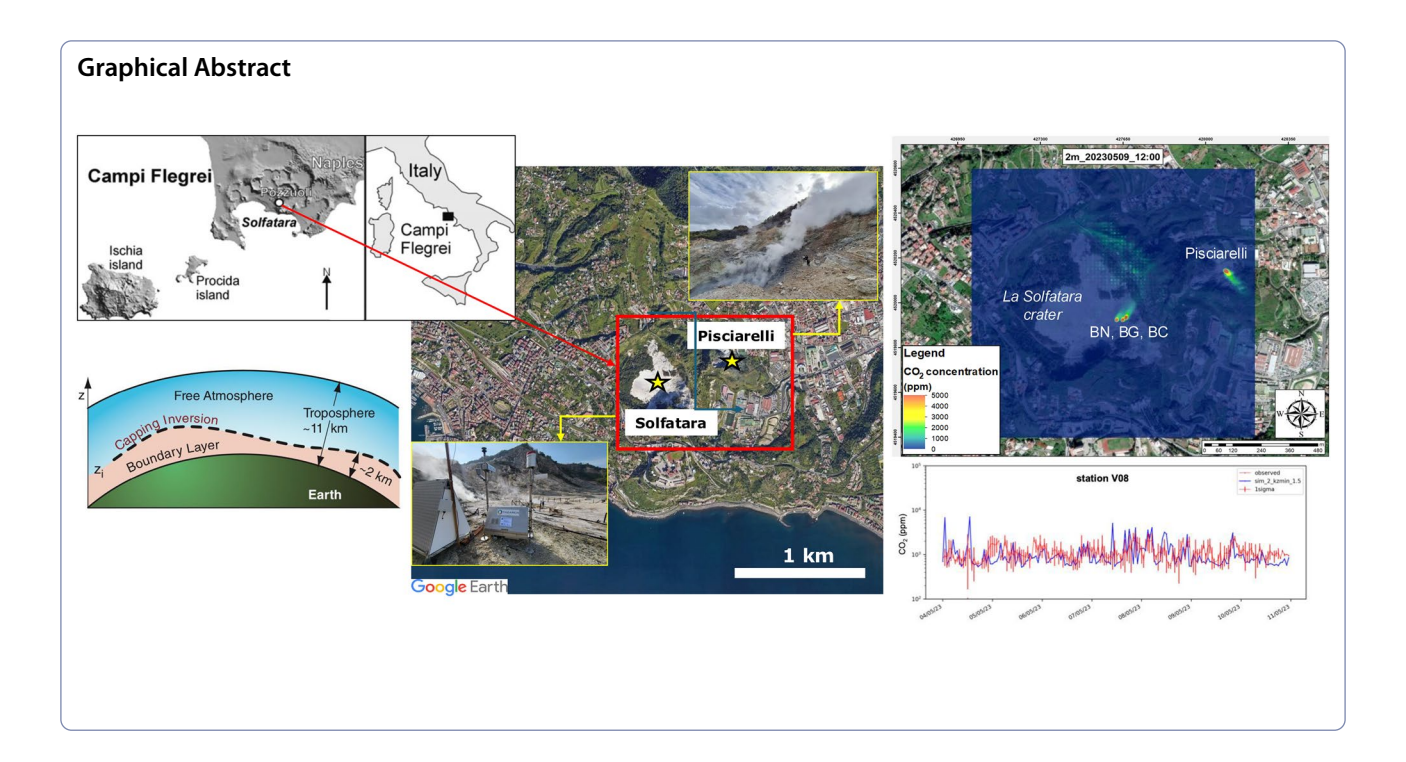
Abstract

Numerical models are widely used to simulate volcanic gas dispersion and estimate local emission sources. However, significant uncertainties arise from the approximations inherent in their physical formulations. Recent advances in high-performance computing (HPC) have enabled high-resolution simulations with minimal numerical diffusion, revealing previously unnoticed limitations in the Monin-Obukhov Similarity Theory used within atmospheric gas dispersion models. One key issue is the determination of the minimum vertical turbulence diffusion coefficient (Kz_{min}) in the atmospheric surface layer (ASL), which plays a crucial role in reducing biases in advection-diffusion models caused by inadequate turbulence representation. In this study, we refine the Eulerian passive gas transport model DISGAS (v. 2.5.1) using measured data on fumarolic and diffuse CO₂ fluxes and air concentrations, along with local wind measurements collected during an ad hoc field campaign from 4 to 10 May 2023. To account for uncertainties in gas flow rates and turbulent velocity fluctuations, we conducted a statistically robust set of simulations by varying CO₂ fluxes and Kz_{min} values. Model outputs were compared with in situ CO₂ concentration measurements at fixed monitoring stations. Results indicate that during stable atmospheric conditions, setting Kz_{min} within the range of $1.5-2 \text{ m}^2 \text{ s}^{-1}$ significantly improves agreement with observations and reduces systematic biases in source estimation. These findings refine model parameterization to better represent turbulence under stable atmospheric conditions at La Solfatara crater during the May 2023 survey. Moreover, the proposed methodology can be adopted for automated data assimilation workflows aimed at constraining unknown fumarolic gas source fluxes in other volcanic settings.

Keywords Gas dispersion model, Carbon dioxide, Diffusivity coefficient, Atmospheric turbulence

*Correspondence: Silvia Massaro silvia.massaro@ingv.it Full list of author information is available at the end of the article





1 Introduction

Gas emissions from active volcanoes mainly occur through crater fumaroles and open vents to form visible volcanic plumes and/or as permanently diffuse degassing from soil [e.g., Piton de la Fournaise, Reuniòn Island, Toutain et al. (2002); Furnas, Azores archipelago, Viveiros et al. (2012); Solfatara, Campi Flegrei, Chiodini et al. (2001); Mammoth Mountain, California, Williams-Jones and Rymer (2015)].

Quantifying CO₂ fluxes is crucial for volcanic monitoring, as their variations are related to changes in magmatic activity at depth, offering early indications of volcanic unrest (e.g., Buono et al. 2023; Tamburello et al. 2019). Hence, improving methods for CO₂ flux estimations can be generally beneficial to volcanic hazards assessments. Moreover, robust forecast of volcanic gas dispersion through numerical models is useful to quantify the evolution of CO2 atmospheric concentrations, which, for high values, can become a hazard for human lives and the environment. Several studies aimed at describing gas transport in volcanic areas (e.g., Heard et al. 2012; Granieri et al. 2015; Heaviside et al. 2021) demonstrate that gas dispersion mainly depends on emission rate, source location, local wind conditions, and turbulence inside the Atmospheric Surface Layer (ASL) (e.g., Granieri et al. 2013; Massaro et al. 2021; Viveiros et al. 2023; Rave-Bonilla et al. 2023).

A common framework for representing turbulent transport in the ASL is the so-called K-theory approach, which is widely used in both observational and modeling

studies of the atmospheric boundary layer (ABL) (e.g., Teixeira and Chienet 2004). In particular, it forms the basis for estimating the vertical turbulence diffusion coefficient K_z under different stability regimes (e.g., Kumar and Sharan 2012) through the Monin–Obukhov Similarity Theory (MOST; Monin and Obukhov 1954) where K_z is typically parameterized as a function of the friction velocity u* and the Monin–Obukhov length L (e.g., Monin and Obukhov 1954; Sharan and Kumar Yadav 1998; Foken 2006; Costa and Macedonio 2016).

However, MOST tends to predict turbulence diffusivity values which are much lower than those effectively observed during stable atmospheric conditions. A few studies were focused on estimating the minimum threshold for the vertical eddy diffusion coefficient, that is Kz_{min} , needed for a less biased estimation of pollutant concentrations in the ABL (e.g., Zhang et al. 2006; Lee et al. 2009; Makar et al. 2014; Ding et al. 2021; Kim and Kim 2024). Indeed, most atmospheric dispersion models cannot accurately simulate diffusion under weakened turbulence (Kumar and Sharan 2012), especially under the nocturnal stable boundary layer (e.g., Sun et al. 2012; Cerenzia 2017; Lan et al. 2022). Such an underestimation of the minimum turbulent diffusivity often results in overestimation of air pollutants concentrations near the surface (e.g., Liu et al. 2020).

A recent study by Kim et al. (2021) showed that reducing Kz_{min} values resulted in overestimation of surface PM2.5 concentrations in Northeast Asia, showing contrasting results with observations. A similar effect

has been also found in the previous version of the passive gas model DISGAS (v.2.5.1; Costa and Macedonio 2016) which assumed a default zero value for the minimum Kz_{min} . So far, these effects on advection–diffusion models have not been critical as, due to computational limitations, the typical used coarse grid resolution could generate significant numerical diffusion caused by truncation error (Leonard 1979; Arampatzis et al. 1994). However, as computational power has significantly increased in recent years, this effect has become clearer (e.g., Syrakos et al. 2012). It is also likely that more advanced methods (e.g., Large Eddie Simulations LES, Implicit Large Eddy Simulation, ILES) or novel algorithms (e.g., Gourianov et al. 2025) that are nowadays prohibitive for operational applications will replace the current one.

Here, we aim to improve the parameterization used in the advection—diffusion model DISGAS by calibrating the minimum turbulent diffusivity, using CO_2 air concentration measurements carried out at La Solfatara crater and Pisciarelli vent (Campi Flegrei, Italy) during an ad hoc gas survey from 4 to 10 May 2023. This area presents unique challenges due to its persistent fumarolic degassing, complex topography and shallow degassing sources. Here, a tailored calibration is essential to robustly quantifying the CO_2 fluxes based on air concentration measurements. Variations in these fluxes can offer valuable insights into changes within the volcanic system, making this approach a useful tool for monitoring the evolution of volcanic unrest (Chiodini et al. 2021).

 ${
m CO_2}$ was selected as the target gas due to its abundance in hydrothermal volcanic emissions and its chemical stability in the atmosphere which makes it less affected by scrubbing processes (unlike ${
m H_2S}$ or ${
m SO_2}$). Moreover, at Campi Flegrei, ${
m CO_2}$ is the dominant gas phase and its flux is continuously and efficiently measured with portable infrared sensors (e.g., Tamburello et al. 2019) as indicator of volcanic activity.

Simultaneous measurements of local meteorological data and diffusive CO_2 flow rate were used as input data for the numerical simulations. Comparing the acquired measurements with model results, we demonstrated that, without setting a minimum threshold for atmospheric diffusion, the DISGAS (v.2.5.1) model tends to

systematically overestimate CO_2 concentrations during stable atmospheric conditions. In order to overcome such a bias, we carried out a sensitivity study using different minimum values of the eddy diffusion coefficient Kz_{min} . The analysis of such results allowed us to statistically estimate the optimal value of such coefficients and so a more robust quantification of the gas source conditions. In the following, we describe the volcanic degassing at La Solfatara area (Sect. 1), the survey data, the methods used to estimate the CO_2 flow rates in the field, and the numerical modeling to reproduce the observations (Sect. 2). Results regarding the characterization of the meteorological measurements, the model outputs, and the statistical calibration are provided (Sect. 3) and then discussed (Sect. 4).

1.1 Volcanic degassing in the area of La Solfatara

La Solfatara is a tuff cone located in the central part of Campi Flegrei caldera which hosts one of the largest fumarolic fields of the world (e.g., Caliro et al. 2007; Fig. 1a).

The persistent degassing poses a potential hazard not only within the crater itself but also to the surrounding densely populated urban areas, where the accumulation of volcanic gases under unfavorable meteorological conditions could lead to concentrations exceeding health risk thresholds. A fatal accident occurred in September 2017, when an Italian family falling into a pit at Solfatara crater immediately died after having inhaled the volcanic gases (https://www.bbc.com/news/world-europe-41243134; last access July 2024). Since then, the access to La Solfatara is very limited, under authorization, exclusively for scientific and monitoring purposes.

There is a large consensus among researchers that injections of deep hot and oxidized fluids into the hydrothermal system of Campi Flegrei cause chemical—physical macroscopic changes in fumarolic activity (Chiodini et al. 2008; Caliro et al. 2025) and fluid-pressure increment in the system, causing ground uplift and $\rm CO_2$ increase in soil degassing (Cardellini et al. 2017) and fumarolic discharges (Caliro et al. 2007; Chiodini et al. 2012; Aiuppa et al. 2013; Tamburello et al. 2019). Since February 2023, escalation in seismicity and surface gas emissions has occurred (INGV 2023; Giudicedipietro

(See figure on next page.)

Fig. 1 a Map showing La Solfatara crater and Pisciarelli site (Campi Flegrei, South Italy; Map data © 2022 Google). Overlapped 50 m-resolution gridded CO_2 diffusive degassing map is shown. The color scale reports the gas flow rate in g m⁻² d⁻¹. The active fumarolic vents (Bocca Nuova, BN: 427,622.91 E, 4,519,924.45 N; Bocca Grande, BG: 427,648.52 E, 4,519,920.63 N, Bocca C, BC: 427,661.88 E, 4,519,933.44 N), Pisciarelli: 428,084 E, 4,520,147 N) are indicated as blue circles, the sonic anemometer (WS: 427,819.82 E, 4,519,842.17 N) as yellow square, and the gas sensors (V202: 427,539.39 E, 4,520,023.66 N; V11: 427,637.55 E, 4,519,942.92 N; V08: 428,099.22 E, 4,520,144.22 N) as red stars. The coordinates are in UTM-WGS84 zone 33; **b** Photo of the present-day plume at Pisciarelli site; **c−e** Photo of the station V11, V202, and V08, respectively (courtesy of Dr. Francesco Rufino)

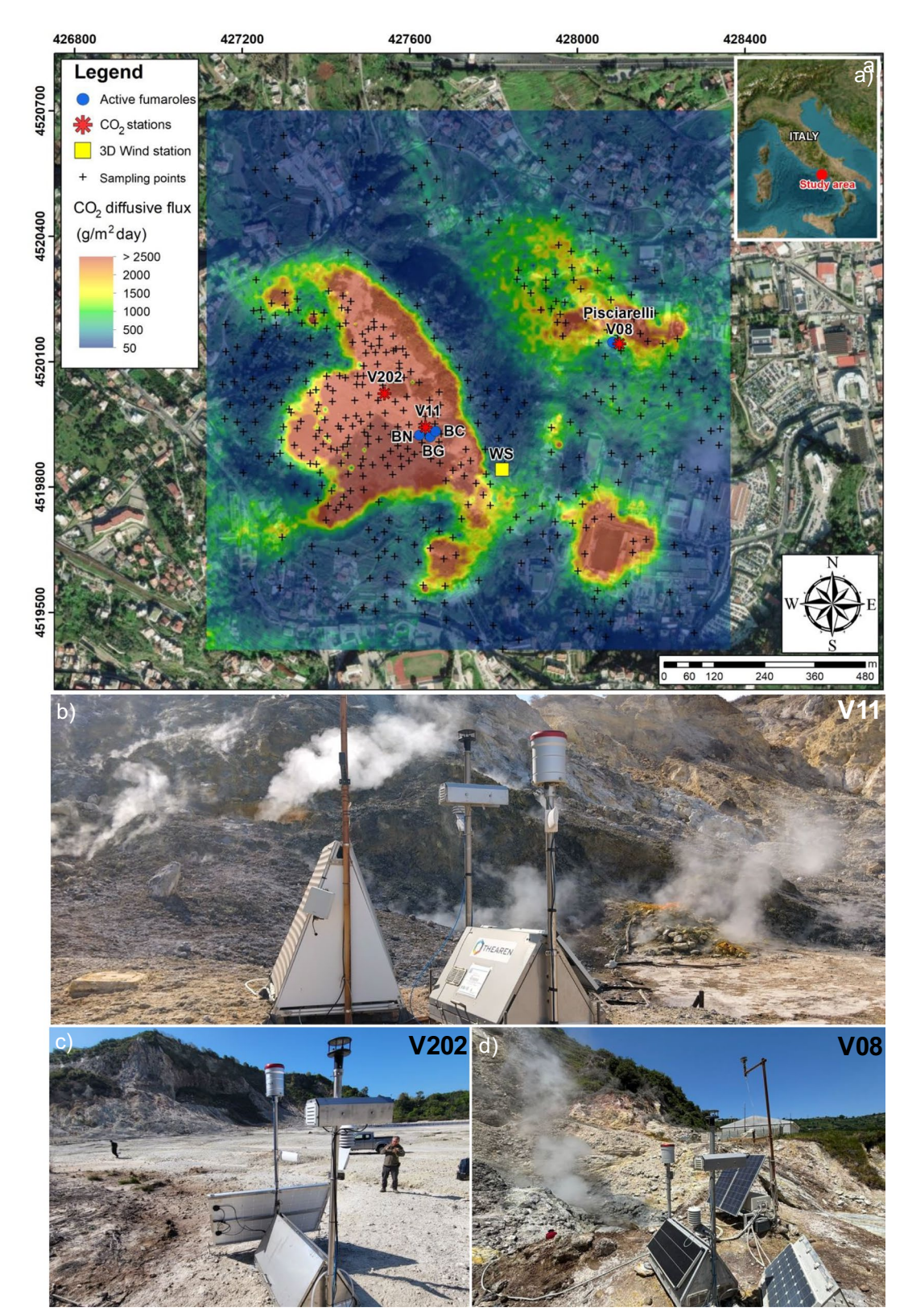


Fig. 1 (See legend on previous page.)

et al. 2025), likely triggered by the central shallow intrusion at about 3.5 km depth (e.g., Giacomuzzi et al. 2024 and reference therein), posing the Civil Protection alert level to "yellow" which indicates increased volcanic monitoring and preparedness without immediate dan-(https://rischi.protezionecivile.gov.it/it/vulcanico/ ger vulcani-italia/campi-flegrei/la-pianificazione-nazionaledi-emergenza-il-rischio-vulcanico-i-campi-flegrei/; access: July 2024). Typically, at La Solfatara and Pisciarelli sites fumarolic gases have H₂O as the main component, followed by CO₂ and minor amounts of H₂S, N₂, H₂, CH₄, He, Ar, CO (see Table 1 in Caliro et al. 2007). On the other hand, SO₂, HCl, and HF are not detectable, due to the scrubbing of magmatic gases within the hydrothermal system (i.e., Cioni et al. 1984; Chiodini et al. 2001).

Generally, the area is affected by widespread soil $\rm CO_2$ release from the Diffuse Degassing Structures area (DDS, Chiodini et al. 2001; Cardellini et al. 2017) of $\sim 1.4~\rm km^2$ including La Solfatara crater where many fault structures dissecting the entire caldera were identified (e.g., Capuano et al. 2013; Cardellini et al. 2017). Significant amounts of $\rm CO_2$ are also emitted by the most active fumarolic vents within the crater called Bocca Grande, Bocca Nuova (BG, BN) and Bocca C (BC, which is a vigorous vent opened in 2008 (Aiuppa et al. 2013) with $\rm CO_2$ emission up to $\sim 300~\rm t~d^{-1}$ in 2013; Aiuppa et al. 2013; Pedone et al. 2014) and in the eastern slope (Pisciarelli vent with $\rm CO_2$ emission up to 600 t d $^{-1}$ in 2019; Tamburello et al. 2019; Fig. 1a).

Chiodini et al. (2021) computed that the total $\rm CO_2$ emissions from the Solfatara DDS increased from ~1000 t d⁻¹ in 2008–2010 up to 3000–4000 t d⁻¹ in 2019–2020. However, recent measurements of diffusive $\rm CO_2$ carried out by the Osservatorio Vesuviano indicate a decreasing flux of ~50% at Solfatara and Pisciarelli (INGV report, July 2024; https://www.ov.ingv.it/index.php/monitoragg io-e-infrastrutture/bollettini-tutti/boll-sett-flegrei/anno-2024; last access July 2024).

A recent geochemical survey of air quality during January and June 2020 in proximity of Pisciarelli, described by Biagi et al. (2022), showed the occurrence of anomalously high CO_2 and H_2S concentrations at the near-surface level, clearly related to the hydrothermal discharges. Although CO_2 concentrations in air remained below the alert threshold of 0.5% (OSHA 2019), the H_2S concentrations were up to two orders of magnitude higher than those of the urban background (1–3 μ g m⁻³; Kourtidis et al. 2008), occasionally exceeding the threshold values suggested by the WHO (2000) for prolonged exposures, i.e., 150 μ g m⁻³ for exposures up to 24 h, 100 μ g m⁻³ for exposures longer than 14 days, and 20 μ g m⁻³ for exposures longer than 90 days (average values during the period).

2 Survey data and methods

2.1 CO₂ flow rate surveys, gas-air concentration measurements, and weather conditions

Measurements of diffuse soil flux using the accumulation chamber method were conducted as outlined by Chiodini et al. (1998). Employing four instruments across four teams, each one equipped with non-dispersive infrared (NDIR) sensors (LICOR) for CO_2 detection, allowed us to simultaneously cover multiple areas. Moreover, the instrument used to measure fluxes in the areas with the highest emission, was also equipped with a SprintIR®-R20 CO_2 sensor with a detection limit ten times higher than the others (2% vs. 20%), in order to have more reliable measurements in those areas. Utilizing a sequential Gaussian simulation algorithm (Cardellini et al. 2003), we interpolated the data and calculated a total CO_2 flow rate of 2130 ± 170 t d $^{-1}$ (Fig. 1a).

Local weather data were acquired with different types of anemometers:

- i. a new Delta Ohm HD2003 ultrasonic static anemometer (WS; Fig. 1a) for measuring wind speed and direction (u-v-w Cartesian components of speed), sound speed, and sonic temperature at a fixed height of ~2 m above ground, equipped with complementary sensors for air temperature, relative humidity, and atmospheric pressure. The RS-232 interface allowed data acquisition at 20 Hz;
- ii. two Gill WindSonic75 high-speed anemometers (Thearen™) installed at the stations V11 and V202 (Fig. 1b and c) and another one at V08 (Fig. 1d). These instruments provide 2D wind data at a fixed height of~2 m above ground without vertical profiling capabilities;
- iii. The Gill WindSonic77 anemometers are equipped with some different kind of CO₂ concentration sensors at 2 m from the ground: (i) Vaisala GMP343 sensor (5000 ppm) placed on V11 and V202 stations, along with the temperature relative humidity sensor (Sensirion™, model SHT35-DIS-F) and pressure sensor (TE Connectivity™, model MS583702BA01-50), (ii) Edinburg GasCard NG sensor (5000 ppm) placed on V08 station with complementary sensors for air temperature, relative humidity and atmospheric pressure. All geochemical stations belong to the geochemical monitoring network of the Osservatorio Vesuviano.

The gas flow rate from fumarolic sources is generally hard to estimate because of the limit of the accumulation chamber method (Chiodini et al. 1998) and the measurement campaigns are generally less frequent. To overcome this issue, here we assessed it within the most likely

ranges of fumarolic flow rates from the active sources (BG, BN, BC and Pisciarelli; Fig. 1a) obtained from the past data acquired in the period from 2012 to 2020 (Aiuppa et al. 2013; Pedone et al. 2014; Tamburello et al. 2019; Chiodini et al. 2021).

For these purposes, for each active source, we calculate the ratio between the fumarolic flow rate (Φ_f) at the three vents and the total diffusive flow rate (Φ_d) from the DDS area for the nearest available period (i.e., during the same year). In Table 1 we reported the variability of the ratio (Φ_f/Φ_d) for each source, obtained considering all

available data provided during the past gas surveys. To obtain the range of the fumarolic flow rates to use in the simulations, we considered a uniform distribution ranging from the minimum to the maximum value of Φ_{d} , while for the related uncertainties, we accounted for the variability (2 σ) of total diffusive flow rate estimated during the last survey (May 2023; see Table 2).

2.2 Gas transport model

DISGAS is an Eulerian model aimed to simulate the passive dispersion of gases in the ABL over large and

Table 1 a) Averaged Φ_d of CO₂ emitted from the DDS area and Φ_f from the active sources (Fig. 1a) during different gas surveys (Aiuppa et al. 2013; Pedone et al. 2014; Cardellini et al. 2017; Tamburello et al. 2019; Chiodini et al. 2021); b) Calculated ratios Φ_f/Φ_d for Solfatara and Pisciarelli sources

a)								
Survey	$CO_2 \Phi_d$ (kg s ⁻¹) from DDS	References	Survey	$CO_2 \Phi_f$ (kg s ⁻¹) from BG, BN, BC	References	Survey	$CO_2 \Phi_f$ (kg s ⁻¹) from Pisciarelli	References
June 2012	5.88	Cardellini et al. (2017)	October 2012	2.04	Aiuppa et al. (2013)	February 2015	3.14	Tamburello et al. (2019)
October 2012	6.8	Cardellini et al. (2017)	October 2012	3.54	Pedone et al. (2014)	Jan-Feb 2019	6.94	Tamburello et al. (2019)
May 2013	5.81	Cardellini et al. (2017)	February 2013	2.9	Aiuppa et al. (2013)			
July 2013	4.79	Cardellini et al. (2017)	February 2013	3.65	Pedone et al. (2014)			
September 2013	4.81	Cardellini et al. (2017)	May 2013	3.63	Pedone et al. (2014)			
March 2015	8.78	Cardellini et al. (2017)						
November 2015	6.9	Cardellini et al. (2017)						
December 2020	49.5	Chiodini et al. (2021)						

Solfatara (BG,	BN, BC)	Pisciarelli	
Period	Φ_f/Φ_d	Period	Φ_{f}/Φ_{d}
2012	0.30	2015	0.36
2012	0.52	2015	0.46
2013	0.50	2019	0.14
2013	0.61	Confidence range	[0.14, 0.46]
2013	0.60		
2013	0.63		
2013	0.76		
2013	0.76		
2013	0.62		
2013	0.76		
2013	0.75		
Confidence range	[0.30, 0.76]		

Table 2 Ranges of variability (2 σ uncertainty) for the total Φ_d of CO₂ from DDS area measured in May 2023 survey and for the Φ_f obtained multiplying Φ_d by the minimum, mean, and maximum values of the ratios Φ_f/Φ_d (see Table 1)

location	Min CO ₂ flow rate (kg s ⁻¹)	Mean CO ₂ flow rate (kg s ⁻¹)	Max CO ₂ flow rate (kg s ⁻¹)
DDS area	20.73	24.5	28.57
BG	2.07	4.65	7.23
BN	2.07	4.65	7.23
BC	2.07	4.65	7.23
Pisciarelli	2.90	8.02	13.14

complex topographic domains using terrain-following coordinates by solving the advection-diffusion equation for the gas concentration only (Costa and Macedonio 2016). Such an approach represents an approximation used to reduce the computational costs since the full description of gas dispersion would require solving the coupled equations for air mass, momentum, energy, and gas concentration (e.g., Macedonio and Costa 2002), which are computationally very demanding to solve within the ASL. In the DISGAS model, the wind field can be either provided by a uniform profile (according to the Monin-Obukhov Similarity theory, for relatively small domains) or through the diagnostic wind computational module, named DIAGNO, derived from Douglas et al. (1990). DIAGNO produces a three-dimensional zero-divergence velocity field consistent with the measured values, avoiding artificial generation or loss of mass. Turbulent terms are parameterized according with the K-theory (e.g., Arya 1995; Costa and Macedonio 2016) as discussed in the next section.

The passive dispersion approximation is adequate when the gas is diluted enough, and the validity of such an approximation can be assessed by estimating the Richardson number (Britter and McQuaid 1988; Cortis and Oldenburg 2009; Costa et al. 2013) (Ri) of the emission source:

$$Ri = \frac{1}{v^2} \left(\frac{g'q}{R}\right)^{\frac{2}{3}} = \frac{1}{v^2 R^{\frac{2}{3}}} \sqrt[3]{\frac{g^2 (\rho_g - \rho_a)^2}{\rho_a^2} q^2}, \quad (1)$$

where g' is the reduced gravity acceleration defined as $g(\rho_g-\rho_a)$, ρ_g and ρ_a are the gas and air densities respectively, q is the volumetric flow rate, R is the plume size (e.g., plume radius), and ν is the wind velocity at the reference altitude (i.e., 10 m). For Ri < 0.25 transport is substantially passive, whereas for Ri > 1 is mainly density driven (Cortis and Oldenburg 2009; Costa et al. 2013).

At Solfatara, the passive condition at the source for ${\rm CO_2}$ is verified for both the fumarolic and diffusive

contributions (Costa et al. 2005; Granieri et al. 2013), due to the high emission temperatures that contribute to decrease the gas density according to the ideal gas law.

To estimate Ri, for fumaroles we can refer to the recent gas flow rates from BG, BC, BN, and Pisciarelli ($\sim 9 \text{ kg s}^{-1}$) under typical wind conditions (~2 m s⁻¹ as mean of typical wind velocities during the day and night; Granieri et al. 2013), considering a fumarolic plume radius of ca. 10 m, a CO₂ density of ca. 1.33 kg m⁻³ (at $T \sim 130$ °C, and P=1013 mbar), and air density ~ 1.2 kg m⁻³ (at standard conditions). Under these conditions we have Ri \approx 0.2. For the diffusive degassing, considering the total mean CO_2 flow rate measured in May 2023 (24.6 kg s⁻¹) with a reference plume radius of ~600 m (as large as the crater radius) and a CO₂ density of ~ 1.66 kg m⁻³ (at T ~ 50 °C, and P=1013 mbar), we obtain Ri ≈ 0.05 . Under such typical conditions, the CO2 plume is dispersed passively. However, such conditions can significantly change depending on meteorological variability.

Given the relative abundance in the gas emissions under analysis (see Table 1 in Caliro et al. 2007), we consider CO_2 as the main gas carrier, which, differently than $\mathrm{H}_2\mathrm{O}$ and other species, is also not reactive. The simulation yields concentrations that are expressed as excess with respect to the background CO_2 level in the air, at heights selected by the user.

2.2.1 Theoretical framework

As we mentioned above, for atmospheric dispersion studies, turbulent flow rates are commonly described using the K-theory, an empirical approach for parameterizing turbulent exchange processes within the atmospheric boundary layer. The basic idea is to express turbulent flow rates (e.g., heat, moisture, momentum) as a product of a turbulent exchange coefficient (often denoted K) and the vertical gradient of the respective variable. According to such an approach, the turbulent flow rate can be expressed in terms of gradients of average concentrations c (e.g., Costa and Macedonio 2016):

$$\overline{u_x'c'} = -K_x \frac{\partial \overline{c}}{\partial_x}; \quad \overline{u_y'c'} = -K_y \frac{\partial \overline{c}}{\partial_y}; \quad \overline{u_z'c'} = -K_z \frac{\partial \overline{c}}{\partial_z},$$
(2)

where u_x , u_y , u_z represent the mean components of the wind velocity in the x (east), y (north), and z (vertical) and w_x , w_y , w_z represent their turbulent fluctuations. The wind field is then written as $V = (u_x + w_x, u_y + w_y, u_z + w_z)$. K = (Kx, Ky, Kz) is the turbulent diagonal diffusivity tensor (Toon et al. 1988; Jacobson et al. 1996; Park and Kim 1999).

It is important to note that while *K*-theory provides a simple and practical way to parameterize turbulent flow

rates, it has limitations, especially in stable atmospheric conditions where it may not accurately represent the complex nature of turbulent processes (e.g., Sharan and Kumar Yadav 1998). Following these considerations, the advection—diffusion equation can be solved for the gas concentration $c = \bar{c} + c\prime$ and written as

$$\frac{\partial \overline{c}}{\partial t} + \frac{\partial u_x \overline{c}}{\partial x} + \frac{\partial u_y \overline{c}}{\partial y} + \frac{\partial u_z \overline{c}}{\partial z} + \frac{\partial \overline{u_x' c'}}{\partial x} + \frac{\partial \overline{u_y' c'}}{\partial y} + \frac{\partial \overline{u_z' c'}}{\partial z} = Q, \quad (3)$$

where u_x , u_y , u_z are the mean component of the wind and w_x , w_y , w_z the fluctuations, and Q is a source term, i.e., the gas mass flow rate from the ground.

In DISGAS the horizontal component of the turbulent diffusivity tensor $K_h\!=\!K_x\!=\!K_y$ is calculated through the Large Eddy Simulation (LES) approach (e.g., Smagorinsky 1963; Pielke et al. 1992) assuming it proportional to the resolution of the grid cell (Byun and Schere 2006):

$$K_h = \Pr_t \alpha^2 \Delta x \Delta y \sqrt{\left(\frac{\partial u_x}{\partial x} - \frac{\partial u_y}{\partial y}\right)^2 + \left(\frac{\partial u_y}{\partial x} + \frac{\partial u_x}{\partial y}\right)^2},$$
(4)

where $\alpha \simeq 0.28$ is a dimensionless constant empirically determined, Δx and Δy the grid spacing (in DISGAS v.2.6.0), and \Pr_t denotes the turbulent Prandtl number.

The vertical component K_z is estimated through the MOST in terms of the frictional velocity u_* and the Monin–Obukhov length L (e.g., Costa and Macedonio 2016):

$$K_z = \frac{\kappa z u_*}{\phi_h},\tag{5}$$

where κ is the von Karman constant ($\kappa = 0.4$), z is the distance from the ground, and ϕ_h is the dimensionless potential temperature gradient (Byun 1990):

$$\phi_h = \Pr_t + \beta_h \frac{z}{L} \quad \text{for} \quad \frac{z}{L} > 0 \text{(stable condition)}$$

$$\phi_h = \Pr_t \left(1 - \gamma_h \frac{z}{L}\right)^{-\frac{1}{2}} \quad \text{for} \quad \frac{z}{L} < 0 \text{(unstable condition)},$$

$$\phi_h = \Pr_t \quad \text{for} \quad \frac{z}{L} = 0 \text{(neutral condition)}$$
(6)

with β_h =7.8, γ_h =11.6, and $\Pr_t \approx 0.95$. From a practical point of view, L is used to characterize the vertical distribution of temperature and wind speed within the ASL. It is often estimated from air temperature differences following the Bulk Richardson method (Golder 1972) but nowadays can be furnished directly by 3D-sonic anemometers. However, as shown by previous studies (e.g., San Josè et al. 2009; Li and Rappenglueck 2018; Kim and Kim 2024), the estimation of the vertical turbulence diffusivity requires setting a minimum threshold for K_z . In formula,

$$K_z = max \left(\frac{\kappa z u_*}{\phi_h}; \quad K_{zmin} \right). \tag{7}$$

Sensitivity experiments carried out by previous studies (San Josè et al. 2009; Li and Rappenglueck 2018; Kim and Kim 2024) suggest setting the minimum value for Kz_{min} of the order of 1 m² s⁻¹ (0 to 3 m² s⁻¹). As an alternative, more sophisticated approaches, which are, however, computationally more demanding, such as dynamic LES or higher-order closure models, can be employed in atmospheric modeling for a more accurate representation of turbulent flow rates, particularly in complex terrain or under stable conditions (e.g., Lu et al. 2022).

3 Meteorological measurements and parameters estimations

We measured the local meteorological variables with the Delta Ohm HD2003 3-axis static anemometer (Fig. 1). This instrument measures the u-v-w Cartesian components of the wind speed (range 0–70 m s⁻¹, resolution 0.1 m s⁻¹, accuracy 1%), sound speed (range 300-380 m s⁻¹, resolution 0.1 m s⁻¹, accuracy 1%), sonic temperature (range -40-60 °C, resolution 0.1 °C, accuracy ± 1 °C), air temperature (range -40-60 °C, resolution 0.1 °C, accuracy ± 0.2 °C), relative humidity (range 0–100%, resolution 0.1%, accuracy ± 2%), and barometric pressure (range 800-1100 mbar, resolution 0.1 mbar, accuracy ± 0.4 mbar).

An internal compass magneto sensor (range 0–360°, resolution 0.1°, accuracy \pm 1°) allows an automatic alignment to magnetic north. The acquisition rate is set at 50 Hz and data are transmitted via RS232 to a Raspberry board and stored in situ into a SD card. The system was powered with two 12 V and 40 Ah batteries. An aluminum tripod allowed the anemometer to be installed at \sim 335 cm above the ground.

The deployment site is an exposed ridge located between Solfatara and Pisciarelli fumarolic fields (WS: 427,819.82 E, 4,519,842.17 N; Fig. 1a), at ~175 m a.s.l. The acquired meteorological variables listed above allowed us to calculate the friction velocity u_* and the Monin–Obukhov length L. To do this we had first to convert the measured variables in order to obtain those needed for atmospheric turbulence calculations, such as the specific humidity q, which is the ratio of water vapor mass m_{ω} to the total (i.e., including dry m_d) air mass m (namely, $m = m_{\omega} + m_d$).

Specific humidity can be calculated from

$$q = 0.622 \cdot \frac{e}{(p - 0.378 \cdot e)},\tag{8}$$

where p is the atmospheric pressure and e is the partial water vapor pressure, obtained from

$$e = \psi e_s, \tag{9}$$

where e_s is the saturation vapor pressure at a given temperature T and ψ is the relative humidity. We then calculate the virtual potential temperature using

$$\theta_{\nu} = T \cdot (1 + 0.608 \cdot q) \cdot \left(\frac{1000}{p}\right)^{0.286}.$$
 (10)

The turbulent components of wind speed u'-v'-w' and temperature are calculated from the following equations:

$$u' = u - \overline{u}$$

$$v' = v - \overline{v}$$

$$w' = w - \overline{w}$$

$$T' = T - \overline{T},$$
(11)

where u, v, w, T are instantaneous values and \overline{u} , \overline{v} , \overline{w} , \overline{T} are averages on a time window of 60 min. We can

calculate the friction velocity u_* and turbulent temperature T_* as

$$u_* = \left[\left(u'w' \right)^2 + \left(v'wv \right)^2 \right]^{0.25},$$
 (12)

$$T_* = \frac{\overline{-w'T'}}{u_*}. (13)$$

Finally, the Monin-Obukhov length scale is obtained from

$$L = \frac{-u_*^3}{k_\nu g \frac{\overline{(w'\theta_\nu)_0}}{\overline{\theta_\nu}}},\tag{14}$$

where k_{ν} the von Karman constant (0.4), g is the gravitational acceleration, $\bar{\theta}_{\nu}$ is the mean virtual potential temperature (in Kelvin), and $(w'\theta_{\nu}')_0$ is the surface value of the kinematic heat flow rate density. Figure 2 shows the variations of u_* and L with time during the period

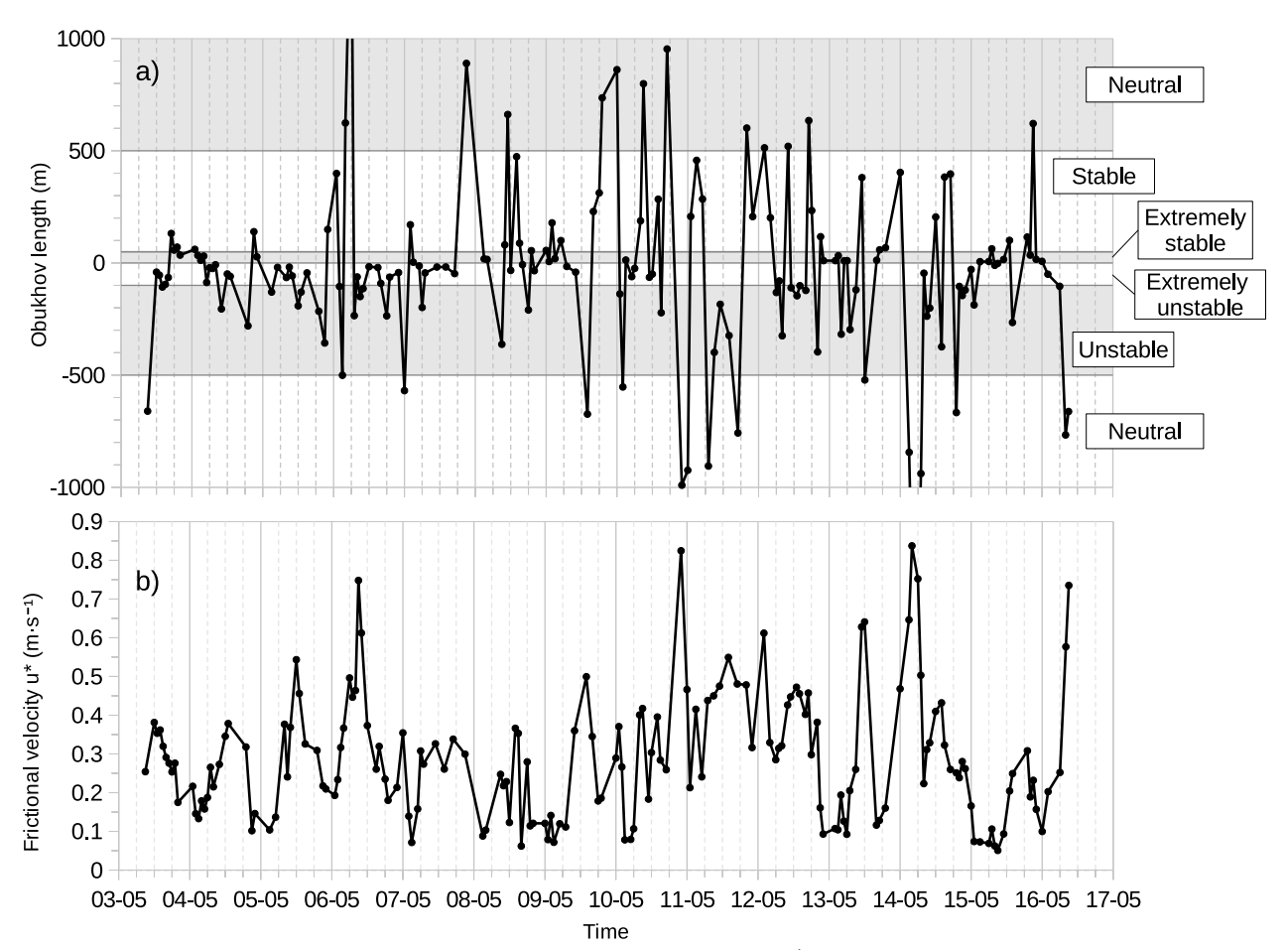


Fig. 2 Variability of **a** the Monin–Obukhov length L (m) and **b** the frictional velocity u_* (m s⁻¹) acquired during the gas survey, from 3 to 16 May 2023 (provided using R library)

of measurement acquisition. The atmospheric conditions appear to be unstable for -500 m < L < 0, stable for 0 < L < 500 m (extremely stable if < 50 m) and neutral if L > |500| m (Sathe et al. 2010).

3.1 Model setup

Our numerical simulations are run using a 3D computational domain composed of a 1200 m×1200 m area discretized with a horizontal resolution of 5 m×5 m (Fig. 1a) having a vertical height of 30 m of variable resolution. The topography is obtained by a 1 m-resolution Digital Elevation Model (courtesy of Osservatorio Vesuviano) and it is characterized by uneven terrain and natural obstacles (e.g., craters, rocks, vegetation), but with no artificial structures. The wind field is generated by diagnostic wind module DIAGNO using the local weather data provided by the sonic anemometers (Fig. 1b-d). The gas source is composed by both the diffusive CO₂ flow rate, averaged over an equally spaced grid of 50 m horizontal resolution, and by the fumarolic contributions emitted as single point sources (BN, BG, BC, and Pisciarelli; Fig. 1a; Table 2).

In order to improve the parameterization used in DISGAS by calibrating the minimum vertical turbulence diffusion coefficient through ${\rm CO_2}$ air concentration measurements, we reproduced the observed ${\rm CO_2}$

concentration (ppm) at 2 m above the ground from 4 to 10 May 2023 by the three geochemical stations (V11, V202, V08; Fig. 1a).

The temporal resolution for the wind data and concentration is set to 1 h, according to the restrictions due to the DIAGNO wind model (Douglas et al. 1990). In order to account for the uncertainties related to the measurements of gas flow rates in the study area, we considered three gas scenarios represented by the mean, the minimum, and the maximum $\rm CO_2$ diffusive flow rate from the DDS area (Table 2), to which we added five different estimations of the fumarolic flow rates representative of the previous assessed ranges (Table 2). The resulting fifteen combinations of gas flow rates used for the simulations are summarized in Table 3.

Those fifteen gas flow rate scenarios are simulated varying also Kz_{min} from 0 to 3 m² s⁻¹ for a total number of 95 simulations, which will be used to statistically constrain the optimal configuration in terms of source flow rates and minimum turbulent diffusivity.

3.2 Workflow management

The whole procedure, from meteorological data retrieval, input generation, simulation runs, and processing to post-processing of model outputs, was managed with

Table 3 CO₂ flow rate data used as inputs for numerical simulations. Three sets of simulations are run considering the variability of the CO2diffusive flow rate ($\Phi d \min$, $\Phi d \max$) and the fumarolic flow rate at active sourcessampled from the ranges in Table 2. The total flow rate ($\Phi d \min$ for each of the 15 combinations is also listed.

Min Φ_d	DDS area	BG	BN	ВС	Pisciarelli	Total
Run	$oldsymbol{arPhi}_d$ min	$oldsymbol{arPhi}_f$	${m \Phi}_{\!f}$	$oldsymbol{arPhi}_f$	Φ_f	$oldsymbol{arPhi}_{tot}$
Sim01	20.73	4.66	4.66	4.66	8.02	42.72
Sim02	20.73	2.07	2.07	2.07	2.90	29.85
Sim03	20.73	7.24	7.24	7.24	13.14	55.59
Sim04	20.73	3.00	3.00	3.00	5.00	34.73
Sim05	20.73	6.00	6.00	6.00	10.00	48.73
Mean Φ_d	DDS area	BG	BN	ВС	Pisciarelli	Total
Run	$oldsymbol{arPhi}_d$ mean	$oldsymbol{arPhi}_f$	${m \Phi}_{\!f}$	$oldsymbol{arPhi}_f$	$oldsymbol{\Phi}_{f}$	$oldsymbol{arPhi}_{tot}$
Sim06	24.65	4.66	4.66	4.66	8.02	46.64
Sim07	24.65	2.07	2.07	2.07	2.90	33.77
Sim08	24.65	7.24	7.24	7.24	13.14	59.51
Sim09	24.65	3.00	3.00	3.00	5.00	38.65
Sim10	24.65	6.00	6.00	6.00	10.00	52.65
Max Φ_d	DDS area	BG	BN	ВС	Pisciarelli	Total
Run	$oldsymbol{arPhi}_d$ max	$oldsymbol{arPhi}_f$	${\it \Phi}_{\it f}$	$oldsymbol{arPhi}_f$	$oldsymbol{\Phi}_{f}$	$oldsymbol{arPhi}_{tot}$
Sim11	28.57	4.66	4.66	4.66	8.02	50.56
Sim12	28.57	2.07	2.07	2.07	2.90	37.69
Sim13	28.57	7.24	7.24	7.24	13.14	63.43
Sim14	28.57	3.00	3.00	3.00	5.00	42.57
Sim15	28.57	6.00	6.00	6.00	10.00	56.57

VIGIL workflow (v.1.3.7; Dioguardi et al. 2022). VIGIL is interfaced with both a dilute gas dispersion model (DISGAS v.2.6.0; Costa and Macedonio et al. 2016) and a dense gas flow model (TWODEE-2 v.2.6.0; Folch et al. 2009), both coupled with the mass-consistent diagnostic wind model DIAGNO (Douglas et al. 1990). VIGIL workflow is designed to manage and run a high number of simulations allowing a systematic variation of meteorological data and gas emission conditions and is suitable for probabilistic studies (e.g., Rafflin et al. 2024; Massaro et al. 2024; Dioguardi et al. 2025). VIGIL launches DIAGNO to generate time-dependent terrain-adapted wind fields from either user-provided or retrieved data by the Copernicus ERA5 reanalysis dataset (Hersbach et al. 2018). Based on the wind data and the information on the source emission given by the user, VIGIL estimates the Richardson number for each day of simulation, running DISGAS or TWODEE-2 models. Finally, it processes the simulation results providing empirical cumulative density functions and hazard curves at user-specified locations and, upon user's request, it produces plots of single days and/or hazard and persistence time maps.

3.3 Statistical indexes

The statistical analysis of the simulated data and real observations is needed for the calibration of the model parameters and determining the goodness of fit. To make such an analysis we consider a set of statistical parameters:

The Aida indexes K_A and k_A (Aida 1978) which measure the logarithmic distance between observed and simulated data:

$$K_A = 10^{\left[\frac{1}{N}\sum_{i=1}^{N}\log\left(\frac{x_{o,i}}{x_{s,i}}\right)\right]},\tag{15}$$

$$k_{A} = 10^{\left\{\sqrt{\frac{1}{N}\sum_{i=1}^{N}\log\left(\frac{x_{o,i}}{x_{s,i}}\right)^{2} - \left[\frac{1}{N}\sum_{i=1}^{N}\log\left(\frac{x_{o,i}}{x_{s,i}}\right)\right]^{2}}\right\}},$$
 (16)

where $x_{o,i}$ and $x_{s,i}$ represent the observed and simulated data, respectively. The first Aida index, K_A , is associated to the geometric average of the distribution, and the second, k_A , is related to the geometric standard deviation of the distribution. A good fit is achieved when K_A is close to 1 (ideally within 5%, that is $0.95 < K_A < 1.05$) and k_A as low as possible and ideally < 1.45 (Aida 1978). Index K_A represents the mean scaling factor to ideally match the observed data, and k_A represents the logarithmic mean dispersion between observed and simulated values.

The Mean Bias Error (MBE)

MBE =
$$\frac{1}{N} \sum_{i}^{N} (x_{o,i} - x_{s,i}).$$
 (17)

The sign of MBE suggests whether the simulated values tend on average to overestimate (>0) or underestimate (<0) the observations.

The Symmetric Mean Absolute Percentage Error (SMAPE)

SMAPE =
$$\frac{200}{N} \sum_{i}^{N} \frac{|x_{s,i} - x_{o,i}|}{\left(|x_{s,i}| + |x_{o,i}|\right)}$$
(18)

The SMAPE calculates the percentage error between the observations and simulations.

These statistical parameters are used to find out the best-fit solution of the observed data. To characterize the accordance between the means of observed and simulated data, we also perform the Student's t-test. Considering the null hypothesis H0 (μ observed = μ simulated), we calculate the t-statistics (i.e., the standardized difference between the sample means to the standard error of that difference) and the p-value (i.e., the probability that H0 is true). If the p-value is below a significance threshold, generally set at 0.05, H0 can be rejected, otherwise can be considered statistically acceptable. In the latter case we can also visually compare the simulated and observed cumulative distributions.

4 Results

4.1 Statistical analysis

Since the temporal acquisition of the data is 15 min and the diagnostic wind model DIAGNO, which is used to generate the wind field accounting for the terrain effects from the local meteorological measurements, has a temporal resolution of one hour, we calculate the hourly averages (along with the standard deviations associated to the measurements) to be compared with the hourly simulation outputs over the whole investigation period. The comparison refers to the height of 2 m from the ground since this is the position where the gas sensors were installed on the geochemical stations.

In order to find the optimal configuration in terms of source flow rates and minimum threshold for the turbulent diffusivity, we calculate the statistical indexes (Aida's K_A and k_A , MBE, and SMAPE) for all gas stations (V11, V202, V08). In Table 4 these indicators are shown considering the mean CO_2 diffusive flow rate (Φ_d mean) as input data (Table 3). Generally, the simulations which used the mean value of source flow rates, Φ_d mean, with $Kz_{min} = 1.5 \text{ m}^2 \text{ s}^{-1}$ and $Kz_{min} = 2 \text{ m}^2 \text{ s}^{-1}$ (Sim07 and Sim08) show the best values of Aida's indexes K_A with

Table 4 Statistical indexes (Aida's KA and kA, MBE, SMAPE) comparing the hourlymeans of observed data and the hourly simulated CO_2 concentrations for all gas stations (V11, V202, V08) at varying Kz_{min} (0-3 m² s⁻¹). The gas flow rate input data are set using the mean CO_2 diffusive flow rate (Φ d mean) along with the five fumarolic gas flow rateset for each vent (i.e., Sim06-Sim10)

Mean Φ_d	K _A							k _A						
	Runs (flow rates)↓													
	0	0.5	1.0	1.5	2.0	2.5	3.0	0	0.5	1.0	1.5	2.0	2.5	3.0
Sim06	0.30	0.54	0.72	0.84	0.93	1.01	1.07	3.11	2.16	1.96	1.86	1.79	1.75	1.75
Sim07	0.34	0.66	0.86	0.99	1.08	1.16	1.22	2.6.08	1.78	1.64	1.58	1.54	1.52	1.53
Sim08	0.21	0.47	0.64	0.75	0.84	0.91	0.97	3.40	2.45	2.21	2.08	2.00	1.94	1.93
Sim09	0.27	0.60	0.79	0.92	1.01	1.09	1.15	2.79	1.94	1.77	1.69	1.64	1.61	1.62
Sim10	0.23	0.52	0.68	0.80	0.89	0.96	1.02	3.24	2.26	2.08	1.96	1.89	1.84	1.83
Mean Φ_d	MBE							SMAPE						
$\text{Kz}_{\text{min}} \rightarrow$	Runs (flow rates)↓													
	0	0.5	1.0	1.5	2.0	2.5	3.0	0	0.5	1.0	1.5	2.0	2.5	3.0
Sim06	-6381.26	- 1728.98	-860.99	-512.48	-320.83	- 195.90	-113.09	97.340	63.10	46.79	40.93	38.78	38.26	39.02
Sim07	-3856.84	-754.70	-269.67	<i>−74.56</i>	33.88	104.44	153.49	93.383	52.01	37.19	32.94	32.12	32.73	34.80
Sim08	- 10,862.58	2704.29	- 1452.60	-951.45	-676.03	-497.21	-380.75	114.200	69.38	52.80	46.59	43.94	42.83	43.10
Sim09	-5569.76	-1128.73	-498.07	-244.54	-104.02	-12.71	49.15	104.909	57.36	41.28	36.26	34.85	34.88	36.36
Sim10	-9195.36	-2005.78	-1124.55	-706.31	-476.55	-327.44	-229.11	111.665	64.67	49.87	43.79	41.37	40.50	41.06

the lowest values of k_A , MBE, and SMAPE. For comparison, in Additional file 1 we provide the same calculations using the minimum and maximum values of source flow rates.

Moreover, to evaluate the local performance on the single stations, we calculate the statistical indexes separately, confirming that $Kz_{min} = 1.5 \text{ m}^2 \text{ s}^{-1}$ represents the optimal parameterization far better than the previous default value ($Kz_{min} = 0$) used in DISGAS v.2.5.1 (Table 5).

In fact, $Kz_{min} = 1.5 \text{ m}^2 \text{ s}^{-1}$ provides better results for stations V11 and V202 for every statistical indicator than the one with $Kz_{min} = 0 \text{ m}^2 \text{ s}^{-1}$. Concerning V08, there is ~ 20% of mass overestimation when $Kz_{min} = 1.5 \text{ m}^2 \text{ s}^{-1}$ although lower k_A and MBE, with respect to the case with $Kz_{min} = 0 \text{ m}^2 \text{ s}^{-1}$ (which predicts a mass underestimation of ~ 20%). Overall, this comparison shows how significant the value of Kz_{min} is in our gas dispersal model.

Figure 3 shows the Empirical Density Functions (ECDFs) of the hourly means of observed CO_2 concentration time series, built for the best-fit simulation case using $Kz_{min} = 1.5 \text{ m}^2 \text{ s}^{-1}$ (Sim07, Φ_d mean). The model outputs show a very good accordance with observations when considering all stations (Fig. 3a) also confirming what reported in Table 5: the model shows an underestimation trend (MBE < 0) for the stations within the Solfatara crater (V11–V202) and an overestimation (MBE > 0) at Pisciarelli (V08).

Finally, in order to determine whether the differences between the best-fit simulation and the observed time

Table 5 Statistical indexes (Aida's K_A and k_A , MBE, SMAPE) calculated for each gas station using $Kz_{min} = 1.5 \text{ m}^2 \text{ s}^{-1}$ and the previous default value $Kz_{min} = 0 \text{ m}^2 \text{ s}^{-1}$

stations	K _A	k _A	MBE	SMAPE	
$Kz_{min} = 1.5 \text{ m}^2 \text{ s}^{-1}$					
V11	0.90	1.52	-202.75	32.58	
V202	0.90	1.34	-74.48	20.93	
V08	1.20	1.74	55.89	45.54	
$Kz_{min} = 0 \text{ m}^2 \text{ s}^{-1}$					
V11	0.21	2.46	-7633	118.85	
V202	0.24	2.02	-3004	114.66	
V08	0.81	2.04	-879	45.78	

Both are referred to the total gas flow rate $\Phi_{\rm tot}$ = 33.77 kg s⁻¹ (Sim07, Φ_d mean, Table 3)

series are likely due to natural variability or if they indicate significant changes that warrant further investigation, we apply the two-tailed Student's t-test without specifying the direction of such difference. The stations V11 and V202 show low t-statistics and *p*-values < 0.05, suggesting no significant difference from the mean. Yet, for station V08 slightly higher values of the statistics imply a significant difference from the observed mean.

In Fig. 4 we report the hourly output of the best-fit simulation ($Kz_{min} = 1.5 \text{ m}^2 \text{ s}^{-1}$, Sim07, Φ_d mean; Tables 3, 4) and the hourly means of observed CO₂ concentration for each gas station, from 4 to 10 May 2023.

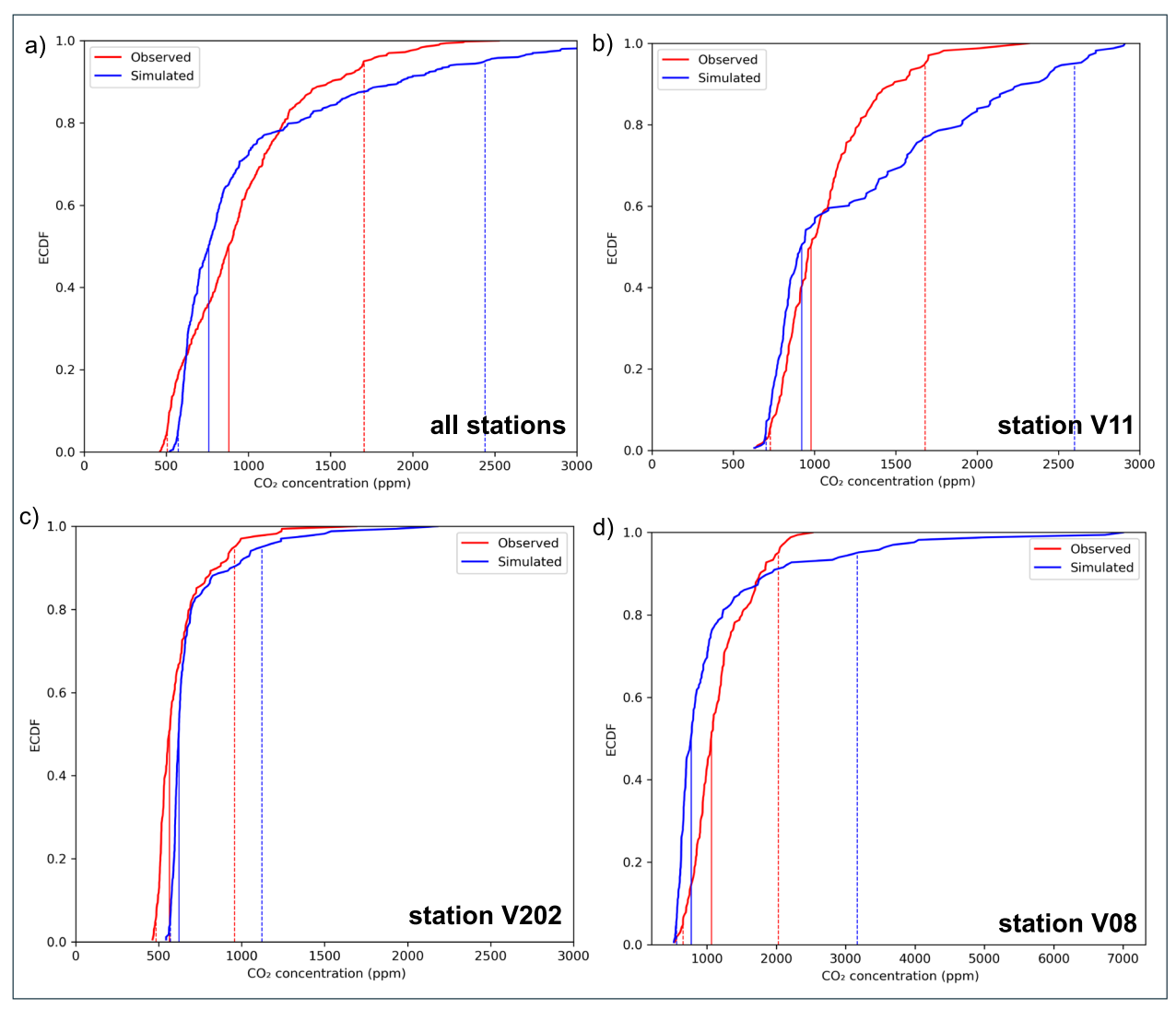


Fig. 3 Empirical Cumulative Density Functions (ECDFs) of the hourly means of observed CO_2 concentration (red curve) and the and hourly simulated one (blue curve) built with the best-fit simulation ($Kz_{min} = 1.5$, Sim07, \mathcal{Q}_d mean, Table 3) at 2 m from the ground are shown for **a** all gas stations, and for each single station **b** V11, **c** V202, **d** V08. The 50° percentile of the ECDF is represented by the vertical solid lines while the 5° and 95° percentiles are represented by the dotted vertical lines (provided using Python library)

In Additional File 2 we provide the same results for $Kz_{min} = 0 \text{ m}^2 \text{ s}^{-1}$ highlighting the bias due to the increased simulated CO_2 concentration at gas stations. At V11 and V202 the outputs (blue curves) are almost one order of magnitude higher than the hourly means of observed data (red curves) during the entire period, while at V08 this increase seems to be limited although there are some very high peaks of the simulated values that overcome the measurements.

5 Discussion

The vertical eddy diffusion within the ASL varies due to numerous factors, including atmospheric stability, diurnal and seasonal variations, turbulence intensity and surface roughness (i.e., vegetation, buildings, and topography). Generally, atmospheric stability affects turbulence diffusion by suppressing vertical mixing while enhancing it in unstable conditions under the influence of the wind shear and thermal convection that increases mixing.

These factors interact in a complex way to determine the value of Kz_{min} at any given time and location, as demonstrated in other models. For instance, Jin et al. (2010)

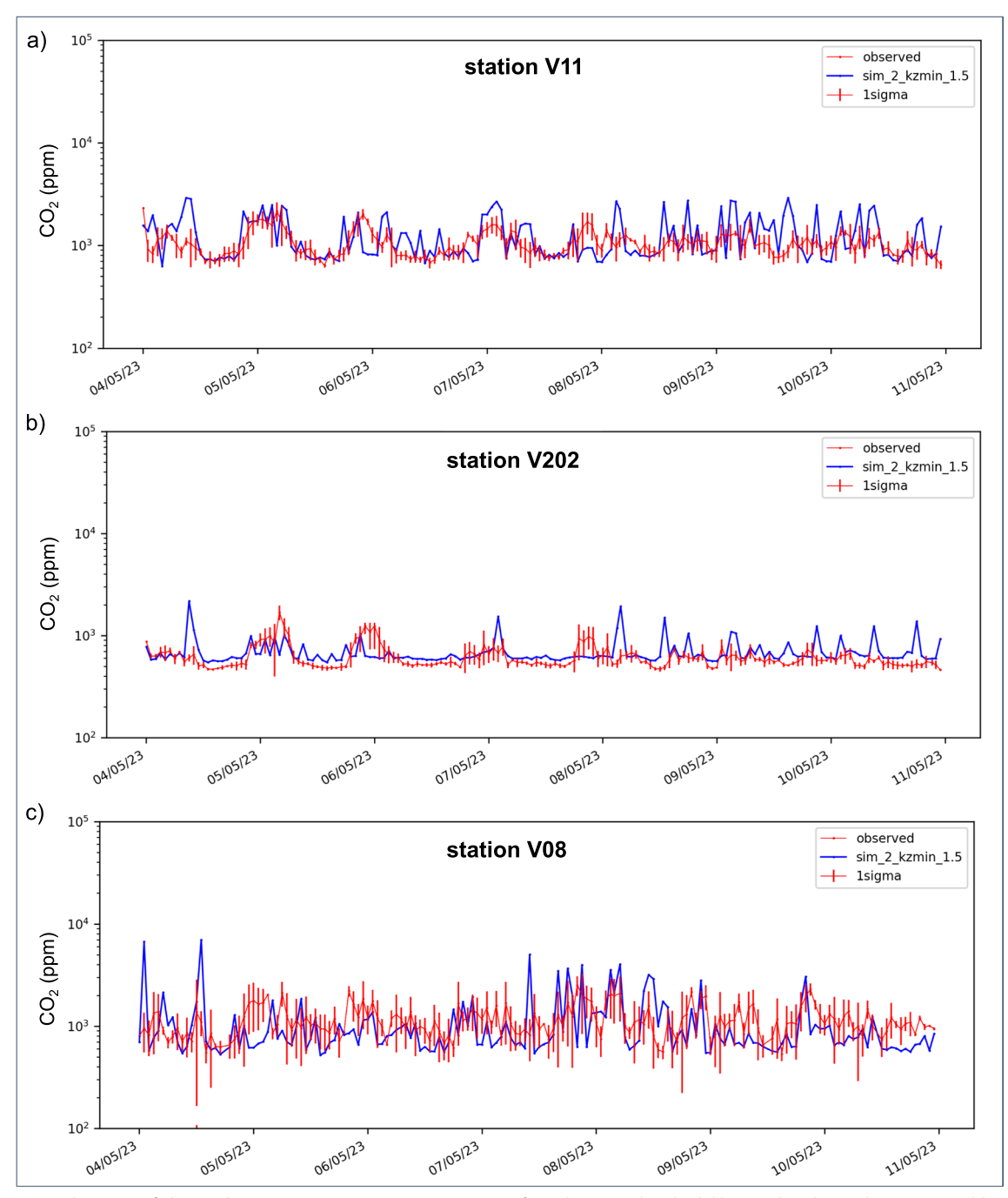


Fig. 4 a) Hourly means of observed Log_{10} CO_2 concentration (ppm) at 2 m from the ground (red solid line) vs. hourly simulation output (blue solid line) considering the best-fit simulation (Kz_{min} = 1.5, Sim07, \mathcal{Q}_d mean, Table 3) for **a** station V11, **b** station V202, and **c** station V08. The red straight lines represent the standard deviation associated with the means of observed data (provided using Python library)

found that the default Kz_{min} =0.5 m² s⁻¹ in the CMAQ model was too high for stable marine layers, causing excessive vertical mixing that led to an increase in surface ozone. More recently, Li and Rappenglueck (2018) compared experiments using a fixed Kz_{min} of 1 m² s⁻¹ and varied values ranging from 0.01 to 1 m² s⁻¹ depending on

land cover, showing that the nighttime ozone bias, for an experiment in Texas, decreased by 31%. Another study carried out by Korsakissok and Mallet (2010) indicated that in urban areas the vertical diffusion is increased due to the turbulence induced by heat and the radiative property of the urban canopy. Thus, the need to increase Kz_{min}

from 0.2 to 0.5 m 2 s $^{-1}$ in order to reduce the overestimation of theemitted pollutants provided by the modelling. More recently, Ding et al. (2021) demonstrated that the change in Kz_{min} exerts a distinct influence on the prediction of the 2 m temperature (T2) which was found to be stronger during the nighttime than during the daytime, in plain areas than in mountain areas, and in urban areas than in non-urban areas. The aforementioned studies highlighted the need of eddy diffusivity parametrizations tailored to the local characteristics of the investigated area (e.g., Kim and Kim 2024).

Thanks to this study we demonstrated that the previous default parameterization for the minimum value of the turbulent diffusion ($Kz_{min} = 0 \text{ m}^2 \text{ s}^{-1}$), used for modeling gas dispersion in volcanic areas, tends to systematically overestimate the CO2 concentration during low-wind, stable atmospheric conditions (Additional file 2). The analysis of the statistical indicators, taking into account all measurement stations, led us to a proper model calibration of Kz_{min} setting its value at 1.5 m² s⁻¹. We then find out the best-fit simulation (Sim07, Φ_d mean; Table 4) showing a good agreement with the hourly means of the observed CO_2 concentration in terms of mass ($K_A \sim 1$, $k_A < 1.75$). In Fig. 5, we showed an example of the simulated CO₂ dispersion map at different periods of simulation during nighttime (07/05/2023, 01:00 a.m. local time; Fig. 5a) and daytime (09/05/2023, 12:00 a.m. local time; Fig. 5b). The increase in gas concentrations observed during the nighttime hours is consistent with reduced atmospheric turbulence, which limits dispersion and favors local accumulation of gas, especially near the fumaroles.

In this regard, in Fig. 6 we show the variation of Kz in the two representative cases of stable and unstable atmospheric conditions (seen in Fig. 5) within the atmospheric boundary layer over the investigated area. Under unstable conditions, Kz generally rapidly increases with height. Conversely, under stable conditions, commonly during the evening or nighttime, surface cooling suppresses turbulence, resulting in lower and more uniform Kz values throughout the ABL. In this regard, the figures clearly demonstrate that Kz remains nearly constant and low in stable conditions, while it increases markedly with height in the unstable case. Setting a minimum value Kz_{min} is needed to ensure a more physically realistic representation of vertical transport within the surface layer, particularly in weakly turbulent conditions. Without it, turbulence could be underestimated under stable conditions, leading to unrealistically low diffusivity values. As we demonstrated, this may result in excessive accumulation of tracers or gases near the ground, which would not be consistent with observed atmospheric behavior and available observations. This is likely due to the very local

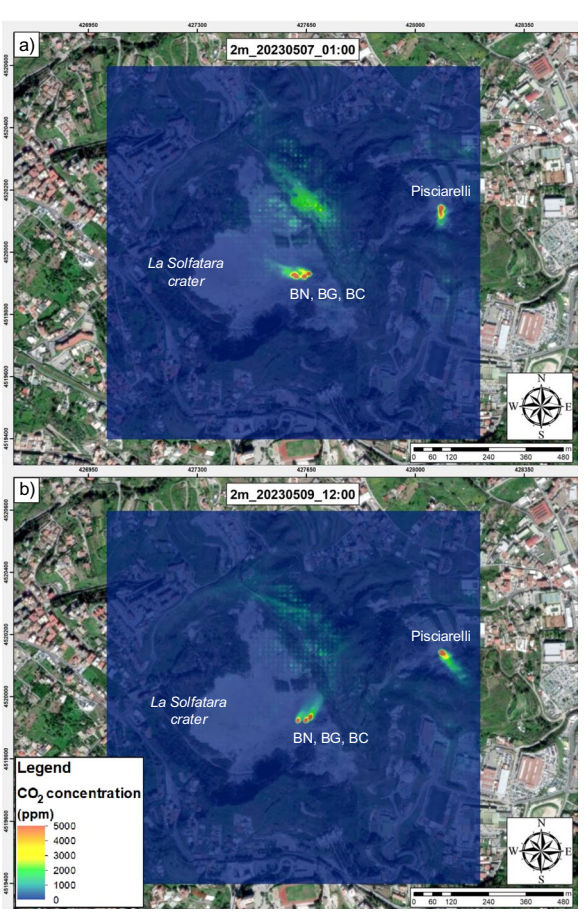


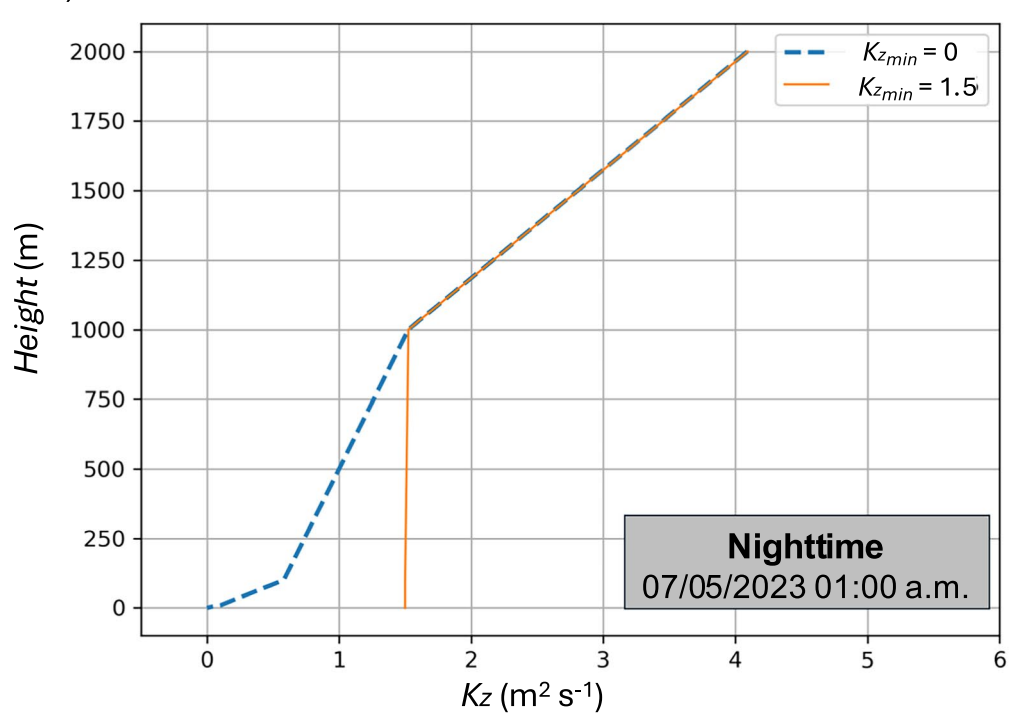
Fig. 5 Map showing the hourly CO_2 simulated concentration using the best-fit simulation ($Kz_{min} = 1.5 \text{ m}^2 \text{ s}^{-1}$, Sim07, Φ_d mean, Table 3) at 2 m from the ground for two periods of simulation: **a** 07/05/2023 at 01:00 a.m. local time and **b** 09/05/2023 at 12:00 a.m. local time. As basemap the La Solfatara crater and Pisciarelli site as provided in Fig. 1 (Map data © 2022 Google)

high temperature anomaly at the surface (e.g., Chiodini et al. 2007; Granieri et al. 2010) where the ground is significantly warmer than the overlying air, which cannot be captured by meteorological models. Such a temperature gradient enhances buoyancy-driven turbulence and vertical mixing, leading to higher values of *Kz* with altitude.

6 Conclusions

Our results indicate that in order to avoid systematic overestimations of the gas concentrations predicted by gas advection—diffusion models during stable atmospheric conditions, a limiting threshold for the eddy diffusion coefficient during stable atmospheric conditions, Kz_{min} , has to be set at ~ 1.5 m² s⁻¹. Although such a correction significantly improves the agreement between model results and observations, this study presents some limitations. For instance, currently we lack observational data to properly describe the surface energy

a) Stable condition



b) Unstable condition

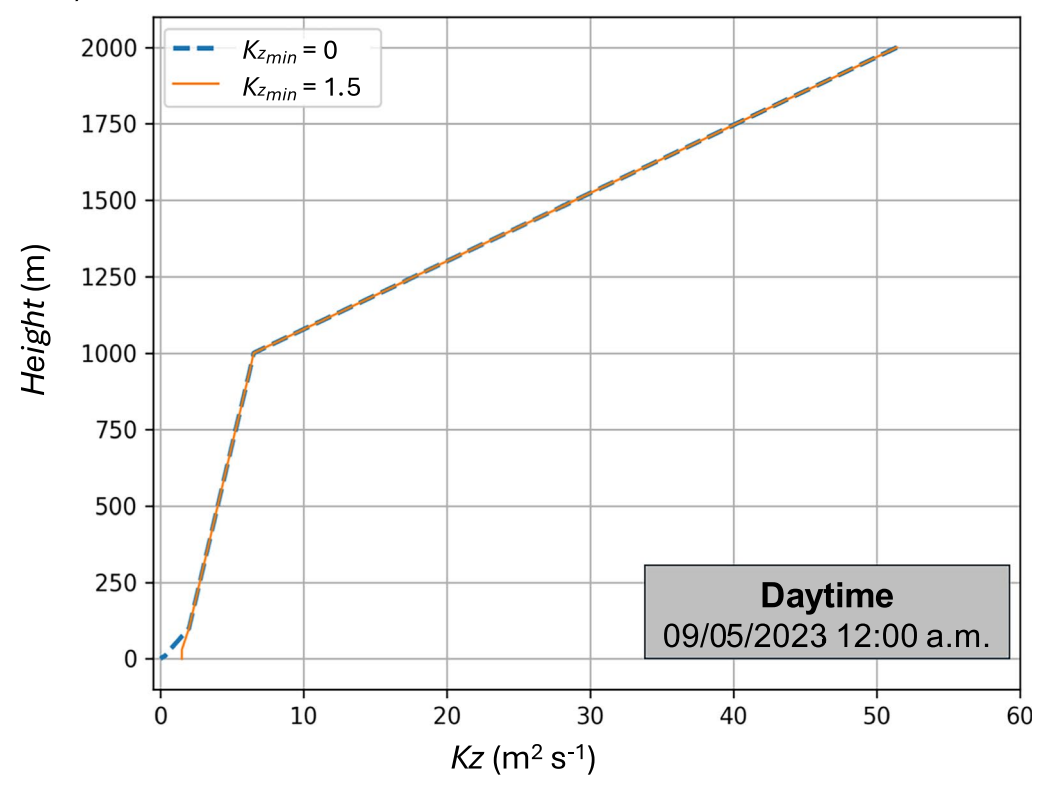


Fig. 6 Typical variation of K_z within the Atmospheric Boundary Layer (ABL) over the computational domain during two typical cases of **a** stable (nighttime; 07/05/2023 at 01:00 a.m. local time) and **b** unstable (daytime; 09/05/2023 at 12:00 a.m. local time) conditions, for $Kz_{min} = 0$ and $Kz_{min} = 1.5$ m² s⁻¹

balance which may help better evaluate the model performance. As reported in Ding et al. (2021) from the energy balance equation, increasing Kz_{min} could cause a significant enhancement of the turbulent mixing within the stable boundary layer at night. Thus, the enhanced mixing in the nighttime reduces the vertical gradient of the potential temperature within the boundary layer and thus elevates the air temperature near the ground surface.

Having the eddy diffusion parameterization properly calibrated, we can use the gas dispersion model DIS-GAS, and the real-time CO_2 air concentration measurements at La Solfatara from the permanent gas and meteorological stations to solve an inverse problem aimed to estimate the volcanic gas fluxes through a statistical analysis. This approach could support the operational management of the gas monitoring surveys and gas hazard at La Solfatara volcano, as well as in other similar areas worldwide.

Abbreviations

ASL Atmospheric surface layer
ABL Atmospheric boundary layer
CMAQ Community Multiscale Air Quality model
DDS Diffusive degassing structures
LES Large Eddie Simulations
ILES Implicit Large Eddie Simulations

MBE Mean bias error

SMAPE Symmetric mean absolute percentage error

Supplementary Information

The online version contains supplementary material available at https://doi.org/10.1186/s40623-025-02272-z.

Additional file 1. Additional file 2.

Acknowledgements

The authors thank the INGV researchers that helped them during the May 2023 gas survey: Emilio Cuoco, Antonio Caradente, and Tullio Ricci. They thank Matteo Cerminara for fruitful discussions on parametrizations of turbulence diffusion.

Author contributions

AC, GM, SC, SM, and GT performed conceptualization and design of the study, analysis, and/or interpretation of data. GM, AC, SM, MS, and FD contributed to coding of the scripts, software, analysis, and interpretation of data. SM, AC, and GT drafted the manuscript. SM, MS, LS, JS, and AC conducted statistical analysis. GT, SC, FR, GB, GC, AS, and RA collected data. AC was involved in coordination of the study and funding. All the authors revised and accepted the submitted version of the manuscript.

Funding

This work has been partially funded by INGV-CPV (Centro di Pericolosità Vulcanica), the European Union's Horizon Europe Research and Innovation Programme (DT-GEO (grant no. 101058129)), and the EuroHPC project ChEESE-2P (grant no. 101093038). FD acknowledges the RETURN Extended Partnership and received funding from the European Union Next-GenerationEU (National Recovery and Resilience Plan—NRRP, Mission 4, Component 2, Investment 1.3—D.D. 1243 2/8/2022, PE0000005).

Data availability

Numerical codes for this research are findable and accessible at the following websites: http://datasim.ov.ingv.it/models/diagno.html; http://datasim.ov.ingv. it/models/disgas.html; https://github.com/BritishGeologicalSurvey/VIGIL.

Declarations

Ethics approval and consent to participate

Not applicable.

Consent for publication

Not applicable.

Competing interests

The authors declare that they have no competing interests.

Author details

¹ Istituto Nazionale di Geofisica e Vulcanologia, Sezione di Bologna, Bologna, Italy. ²Dipartimento di Scienze della Terra e Geoambientali, Università di Bari, Bari, Italy. ³Istituto Nazionale di Geofisica e Vulcanologia, Osservatorio Vesuviano, Ercolano, Italy. ⁴Dipartimento di Scienze della Terra, dell'Ambiente e delle Risorse, Università degli Studi "Federico II", Napoli, Italy. ⁵British Geological Survey, The Lyell Centre, Edinburgh, United Kingdom.

Received: 28 February 2025 Accepted: 10 August 2025 Published online: 16 September 2025

References

Aida I (1978) Reliability of a tsunami source model derived from fault parameters. J Phys Earth 26(1):57–73. https://doi.org/10.4294/jpe1952.

Aiuppa A, Tamburello G, Di Napoli R, Cardellini C, Chiodini G, Giudice G, Grassa F, Pedone M (2013) First observations of the fumarolic gas output from a restless caldera: implications for the current period of unrest (2005–2013) at Campi Flegrei. Geochem Geophys Geosyst 14(10):4153–4169

Arampatzis G, Assimacopoulos D, Mitsoulis E (1994) Treatment of numerical diffusion in strong convective flows. Int J Numer Methods Fluids 18(3):313–331

Arya SP (1995) Modeling and parameterization of near-source diffusion in weak winds. J Appl Meteorol 34:1112–1122

Biagi R, Tassi F, Caliro S, Capecchiacci F, Venturi S (2022) Impact on air quality of carbon and sulfur volatile compounds emitted from hydrothermal discharges: the case study of Pisciarelli (Campi Flegrei, South Italy). Chemosphere 297:134166

Britter RE, McQuaid JD (1988) Workbook on the dispersion of dense gases.

Tech Rep HSE Contract Research Report No. 17/1988, Trinity Road Bootle,
Merseyside L20 3QY, UK.

Buono G, Caliro S, Paonita A, Pappalardo L, Chiodini G (2023) Discriminating carbon dioxide sources during volcanic unrest: the case of Campi Flegrei caldera (Italy). Geology 51(4):397–401

Byun DW (1990) On the analytical solutions of flux-profile relationships for the atmospheric surface layer. J Appl Meteorol. https://doi.org/10.1175/1520-0450(1990)029%3c0652:OTASOF%3e2.0.CO;2

Byun D, Schere KL (2006) Review of the governing equations, computational algorithms, and other components of the models-3 community multiscale air quality (CMAQ) modeling system. Appl Mech Rev 59(2):51–77

Caliro S, Chiodini G, Moretti R, Avino R, Granieri D, Russo M, Fiebig J (2007) The origin of the fumaroles of La Solfatara (Campi Flegrei, south Italy). Geochim Cosmochim Acta 71(12):3040–3055

Caliro S, Chiodini G, Avino R, Carandente A, Cuoco E, Di Vito MA, Minopoli C, Rufino R, Santi A, Lages J, Mangiacapra A, Monteleone B, Pappalardo L, Tarcsak Z, Tramati C, Vizzini S, Aiuppa A (2025) Escalation of caldera unrest indicated by increasing emission of isotopically light sulfur. Nat Geosci 18:1–8

Capuano P, Russo G, Civetta L, Orsi G, D'Antonio M, Moretti R (2013) The active portion of the Campi Flegrei caldera structure imaged by 3D inversion of gravity data. Geochem Geophys Geosyst 14(10):4681–4697

- Cardellini C, Chiodini G, Frondini F (2003) Application of stochastic simulation to CO_2 flow rate from soil: mapping and quantification of gas release. J Geophys Res Solid Earth. https://doi.org/10.1029/2002JB002165
- Cardellini C, Chiodini G, Frondini F, Avino R, Bagnato E, Caliro S, Lelli M, Rosiello A (2017) Monitoring diffuse volcanic degassing during volcanic unrests: the case of Campi Flegrei (Italy). Sci Rep 7:6757. https://doi.org/10.1038/s41598-017-06941-2
- Cerenzia I (2017) Challenges and critical aspects in stable boundary layer representation in numerical weather prediction modeling: Diagnostic analyses and proposals for improvement. PhD Thesis, Alma Mater Studiorum, University of Bologna.
- Chiodini G, Cioni R, Guidi M, Raco B, Marini L (1998) Soil CO₂ flux measurements in volcanic and geothermal areas. Appl Geochem 13(5):543–552
- Chiodini G, Frondini F, Cardellini C, Granieri D, Marini L, Ventura G (2001) CO₂ degassing and energy release at Solfatara volcano, Campi Flegrei, Italy. J Geophys Res Solid Earth 106(B8):16213–16221
- Chiodini G, Vilardo G, Augusti V, Granieri D, Caliro S, Minopoli C, Terranova C (2007) Thermal monitoring of hydrothermal activity by permanent infrared automatic stations: results obtained at Solfatara di Pozzuoli, Campi Flegrei (Italy). J Geophys Res Solid Earth. https://doi.org/10.1029/2007/B005140
- Chiodini G, Caliro S, Cardellini C, Avino R, Granieri D, Schmidt A (2008) Carbon isotopic composition of soil CO_2 efflux, a powerful method to discriminate different sources feeding soil CO2 degassing in volcanic-hydrothermal areas. Earth Planet Sci Lett 274(3–4):372–379
- Chiodini G, Caliro S, De Martino P, Avino R, Gherardi F (2012) Early signals of new volcanic unrest at Campi Flegrei caldera? Insights from geochemical data and physical simulations. Geology 40(10):943–946
- Chiodini G, Caliro S, Avino R, Bini G, Giudicepietro F, De Cesare W, Ricciolino A, Aiuppa A, Cardellini C, Petrillo Z, Selva J, Siniscalchi A, Tripaldi S (2021) Hydrothermal pressure-temperature control on CO₂ emissions and seismicity at Campi Flegrei (Italy). J Volcanol Geotherm Res 414:10724
- Cioni R, Corazza E, Marini L (1984) The gas/steam ratio as indicator of heat transfer at the Solfatara fumaroles, Phlegraean Fields (Italy). Bull Volcanol 47:295–302
- Cortis A, Oldenburg CM (2009) Short-range atmospheric dispersion of carbon dioxide. Boundary-Layer Meteorol 133:17–34. https://doi.org/10.1007/s10546-009-9418-y
- Costa A, Macedonio G, Chiodini G (2005) Numerical model of gas dispersion emitted from volcanic sources. Ann Geophys 48(4–5):805–815
- Costa A, Folch A, Macedonio G (2013) Density-driven transport in the umbrella region of volcanic clouds: implications for tephra dispersion models. Geophys Res Lett 40(18):4823–4827
- Costa A, Macedonio G (2016) A model for passive DISpersion of GAS and particles, Users's Manual DISGAS-2.6.0. http://datasim.ov.ingv.it/models/disgas.html.
- Ding H, Cao L, Jiang H, Jia W, Chen Y, An J (2021) Influence on the temperature estimation of the planetary boundary layer scheme with different minimum eddy diffusivity in WRF v3. 9.1.1. Geosci Model Dev 14(10):6135–6153
- Dioguardi F, Massaro S, Chiodini G, Costa A, Folch A, Macedonio G, Sandri L, Selva J, Tamburello G (2022) VIGIL: a Python tool for automatized probabilistic volcanlc gas dispersion modeLling. Ann Geophys. https://doi.org/10.4401/ag-8796
- Dioguardi F, Chiodini G, Costa A (2025) Probabilistic hazard analysis of the gas emission of Mefite d'Ansanto, southern Italy. Nat Haz Earth Sys Sci 25(2):657–674
- Douglas SG, Kessler RC, Carr EL (1990) User's guide for the Urban Airshed Model. Volume 3. User's manual for the Diagnostic Wind Model. Systems Applications, Inc., San Rafael, CA (USA). https://www.osti.gov/biblio/6110089.
- Foken T (2006) 50 years of the Monin-Obukhov similarity theory. Bound-Layer Meteorol 119:431–447
- Folch A, Costa A, Hankin RK (2009) Twodee-2: a shallow layer model for dense gas dispersion on complex topography. Comput Geosci 35(3):667–674
- Giacomuzzi G, Chiarabba C, Bianco F, De Gori P, Agostinetti NP (2024) Tracking transient changes in the plumbing system at Campi Flegrei caldera. Earth Planet Sci Lett 637:118744
- Giudicepietro F, Avino R, Bellucci Sessa E, Bevilacqua A, Bonano M, Caliro S, Csu F, De Cesare W, De Luca C, De Martino P, Di Traglia F, Di Vito MA, Dolce M, Esposito AM, Lanari R, Macedonio G, Manuta M, Minopoli

- C, Monterroso F, Neri A, Ricciolino P, Rufino F, Santi A, Scarpato G, Straino P, Tramelli A, Chiodini G (2025) Burst-like swarms in the Campi Flegrei caldera accelerating unrest from 2021 to 2024. Nature Comm 16(1):1548
- Golder D (1972) Relations among stability parameters in the surface layer. Bound-Layer Meteorol 3:47–58
- Gourianov N, Givi P, Jaksch D, Pope SB (2025) Tensor networks enable the calculation of turbulence probability distributions. Sci Adv 11(5):eads5990
- Granieri D, Avino R, Chiodini G (2010) Carbon dioxide diffuse emission from the soil: ten years of observations at Vesuvio and Campi Flegrei (Pozzuoli), and linkages with volcanic activity. Bull Volcanol 72:103–118
- Granieri D, Costa A, Macedonio G, Bisson M, Chiodini G (2013) Carbon dioxide in the urban area of Naples: contribution and effects of the volcanic source. J Volcanol Geotherm Res 260:52–61
- Granieri D, Salerno G, Liuzzo M, La Spina A, Giuffrida G, Caltabiano T, Giudice G, Montalvo F, Burton MR, Papale P (2015) Emission of gas and atmospheric dispersion of SO2 during the December 2013 eruption at San Miguel volcano (El Salvador, Central America). Geophys Res Lett. https://doi.org/10.1002/2015GI.064660
- Heard IP, Manning AJ, Haywood JM, Witham C, Redington A, Jones A, Bourassa A (2012) A comparison of atmospheric dispersion model predictions with observations of SO2 and sulphate aerosol from volcanic eruptions. J Geophys Res Atmos. https://doi.org/10.1029/2011JD016791
- Heaviside C, Witham C, Vardoulakis S (2021) Potential health impacts from sulphur dioxide and sulphate exposure in the UK resulting from an Icelandic effusive volcanic eruption. Sci Total Environ 774:145549
- Hersbach H, Bell B, Berrisford P, Biavati G, Horányi A, Muñoz Sabater J, Nicolas J, Peubey C, Radu R, Rozum I, Schepers D, Simmons A, Soci C, Dee D, Thépaut JN (2018) ERA5 hourly data on single levels from 1940 to present. Copernicus Climate Change Service (C3S) Climate Data Store (CDS), https://doi.org/10.24381/cds.adbb2d47. Accessed on 04 Jan 2024.
- INGV (2023) Vesuvius observatory, surveillance bulletins, https://www.ov.ingv. it/index.php/monitoraggio-e-infrastrutture/bollettini-tutti/bollett-mensi li-cf/anno-2023-1.
- Jacobson MZ, Lu R, Turco RP, Toon OB (1996) Development and application of a new air pollution modeling system-part I: Gas-phase simulations. Atmos Environ 30(12):1939–1963
- Jin L, Brown NJ, Harley RA, Bao JW, Michelson SA, Wilczak JM (2010) Seasonal versus episodic performance evaluation for an Eulerian photochemical air quality model. J Geophys Res Atmos. https://doi.org/10.1029/2009J D012680
- Kim E, Kim Y (2024) Determinants of user acceptance of digital insurance platform service on InsurTech: an empirical study in South Korea. Asian J Techn Innov 33(1):45–75. https://doi.org/10.1080/19761597.2024.23376 29
- Kim BU, Kim HC, Kim S (2021) Effects of vertical turbulent diffusivity on regional PM2.5 and O_3 source contributions. Atmos Environ 245:118026
- Korsakissok I, Mallet V (2010) Development and application of a reactive plume-in-grid model: evaluation over Greater Paris. Atmos Chem Phys 10(18):8917–8931
- Kourtidis K, Kelesis A, Petrakakis M (2008) Hydrogen sulfide ($\rm H_2S$) in urban ambient air. Atmos Environ 42(32):7476–7482
- Kumar P, Sharan M (2012) Parameterization of the eddy diffusivity in a dispersion model over homogeneous terrain in the atmospheric boundary layer. Atmos Res 106:30–43
- Lan C, Liu H, Katul GG, Li D, Finn D (2022) Turbulence structures in the very stable boundary layer under the influence of wind profile distortion. J Geophys Res Atmos 127(20):e2022JD036565
- Lee P, Tang Y, Kang D, McQueen J, Tsidulko M, Huang HC, Lu S, Hart M, Lin HM, Yu S, Dimego G, Stajner I, Davidson P (2009) Impact of consistent boundary layer mixing approaches between NAM and CMAQ. Environ Fluid Mech 9:23–42
- Leonard BP (1979) A stable and accurate convective modelling procedure based on quadratic upstream interpolation. Comput Methods Appl Mech Eng 19(1):59–98
- Li X, Rappenglueck B (2018) A study of model nighttime ozone bias in air quality modeling. Atmos Environ 195:210–228
- Liu T, Lin B, Fu X, Gao Y, Kong J, Zhao Y, Song H (2020) Experimental study on gas diffusion dynamics in fractured coal: a better understanding of gas migration in in-situ coal seam. Energy 195:117005

- Lu J, Zhou W, Kong H, Leung LR, Harrop B, Song F (2022) On the diffusivity of moist static energy and implications for the polar amplification response to climate warming. J Clim 35(21):7127–7146
- Macedonio G, Costa A (2002) Finite Element modeling of gas dispersion in the atmosphere. In: Buccianti A, Marini L, Ottonello G, Vaselli O (eds) Proceedings of the Arezzo Seminar in Fluids Geochemistry, 147–159, Pacini Editore, Ospedaletto (Pisa).
- Makar PA, Nissen R, Teakles A, Zhang J, Zheng Q, Moran MD, Yau H, Dicenzo C (2014) Turbulent transport, emissions and the role of compensating errors in chemical transport models. Geosci Model Dev 7(3):1001–1024
- Massaro S, Dioguardi F, Sandri L, Tamburello G, Selva J, Moune S, Jessop DE, Moretti R, Komorowski JC, Costa A (2021) Testing gas dispersion modelling: a case study at La Soufrière volcano (Guadeloupe, Lesser Antilles). J Volcanol Geotherm Res 417:107312
- Massaro S, Tamburello G, Bini G, Costa A, Stocchi M, Tassi F, Vaselli O, Chiodini G, Dioguardi F, Selva J, Sandri L, Macedonio G, Caliro S, Vougioukalakis G (2024) Quantification of volcanic degassing and analysis of uncertainties using numerical modeling: the case of Stephanos crater (Nisyros Island, Greece). Bull Volcanol 86(12):95
- Monin AS, Obukhov AM (1954) Basic laws of turbulent mixing in the surface layer of the atmosphere. Contrib Geophys Inst Acad Sci USSR 151(163):e187
- OSHA (2019) Carbon Dioxide Health Hazard Information Sheet. FSIS Environmental, Safety and Health Group.
- Park FC, Kim JW (1999) Singularity analysis of closed kinematic chains. ASME J Mech des 121(1):32–38. https://doi.org/10.1115/1.2829426
- Pedone M, Aiuppa A, Giudice G, Grassa F, Cardellini C, Chiodini G, Valenza M (2014) Volcanic CO₂ flux measurement at Campi Flegrei by tunable diode laser absorption spectroscopy. Bull Volcanol 76(4):1–13
- Pedone M, Granieri D, Moretti R, Fedele A, Troise C, Somma R, De Natale G (2017) Improved quantification of CO₂ emission at Campi Flegrei by combined Lagrangian stochastic and Eulerian dispersion modelling. Atmos Environ 170:1–11
- Pielke RA, Cotton WR, Walko RL, Tremback CJ, Nicholls ME, Moran MD, Wesley DA, Lee TJ, Copeland JH (1992) A comprehensive meteorological modeling system-RAMS. Meteorol Atmos Phys 49:69–91
- Rafflin V, Boudoire G, Massaro S, Stocchi M, Costa A, Grassa F, Giuffrida G, Gailler L, Liuzzo M, Planche C, Banson S, Harris A (2024) Modelling ${\rm CO_2}$ dispersion in the air during potential limnic eruption at the lake Pavin (France). J Volcanol Geotherm Res 447:108024
- Rave-Bonilla YP, Jessop DE, Moune S, Garbin C, Moretti R (2023) Numerical modelling of the volcanic plume dispersion from the hydrothermal system of La Soufrière de Guadeloupe. Volcanica 6(2):459–477
- San José R, Pérez JL, Morant JL, Prieto F, González RM (2009) Improved modelling experiment for elevated PM10 and PM2.5 concentrations in Europe with MM5-CMAQ and WRF/CHEM. Air Pollut 123:377–386
- Sathe A, Mann J, Gottschall J, Courtney MS (2010) Estimating the systematic errors in turbulence sensed by wind lidars. Risø National Laboratory, Roskilde, Denmark. Risø 24.
- Sharan M, Kumar Yadav A (1998) Simulation of diffusion experiments under light wind, stable conditions by a variable K-theory model. Atmos Environ 32(20):3481–3492
- Smagorinsky J (1963) General circulation experiments with the primitive equations, part I: the basic experiment. Mon Weather Rev 91(3):99–164
- Sun J, Mahrt L, Banta RM, Pichugina YL (2012) Turbulence regimes and turbulence intermittency in the stable boundary layer during CASES-99. J Atmos Sci 69(1):338–351
- Syrakos A, Efthimiou G, Bartzis JG, Goulas A (2012) Numerical experiments on the efficiency of local grid refinement based on truncation error estimates. J Comput Phys 231(20):6725–6753
- Tamburello G, Caliro S, Chiodini G, De Martino P, Avino R, Minopoli C, Carandente A, Rouwet D, Aiuppa A, Costa A, Bitetto M, Giudice G, Francoforte V, Ricci T, Sciarra A, Bagnato E, Capecchiacci F (2019) Escalating CO₂ degassing at the Pisciarelli fumarolic system, and implications for the ongoing Campi Flegrei unrest. J Volcanol Geotherm Res 384:151–157
- Teixeira J, Cheinet S (2004) A simple mixing length formulation for the eddydiffusivity parameterization of dry convection. Bound-Layer Meteorol 110:435–453
- Toon OB, Turco RP, Westphal D, Malone R, Liu M (1988) A multidimensional model for aerosols: description of computational analogs. J Atmos Sci 45(15):2123–2144

- Toutain JP, Baubron JC, François L (2002) Runoff control of soil degassing at an active volcano. The case of Piton de la Fournaise, Réunion Island. Earth Planet Sci Lett 197(1–2):83–94
- Viveiros F, Cardellini C, Ferreira T, Silva C (2012) Contribution of CO₂ emitted to the atmosphere by diffuse degassing from volcanoes: the Furnas Volcano case study. Int J Glob Warm. https://doi.org/10.1504/IJGW.2012.049444
- Viveiros F, Baldoni E, Massaro S, Stocchi M, Costa A, Caliro S, Chiodini G, Andrade C (2023) Quantification of CO₂ degassing and atmospheric dispersion at Caldeiras da Ribeira Grande (São Miguel Island, Azores). J Volcanol Geotherm Res 438:107807
- WHO (2000) Hydrogen sulphide, 2nd edn. Air Quality Guidelines for Europe. WHO Regional Office for Europe, Copenhagen, Denmark.
- Williams-Jones G, Rymer H (2015) Hazards of Volcanic Gases. In: Sigurdsson H (ed) The Encyclopedia of Volcanoes, 2nd edn. Academic Press, pp 985–992. https://doi.org/10.1016/B978-0-12-385938-9.00057-2
- Zhang Y, Liu P, Queen A, Misenis C, Pun B, Seigneur C, Wu SY (2006) A comprehensive performance evaluation of MM5-CMAQ for the summer 1999 Southern Oxidants Study episode—Part II: gas and aerosol predictions. Atmos Environ 40(26):4839–4855

Publisher's Note

Springer Nature remains neutral with regard to jurisdictional claims in published maps and institutional affiliations.